Symmetrical Virtual 48-Pulse Rectifier With Hybrid Multimode Pulse Multiplication for High-Current-Density Hydrogen Electrolyzers

Hanlei Tian, *Student Member, IEEE*, Guozhuang Liang, *Member, IEEE*,
Jinliang Huang, *Student Member, IEEE*, Junyu Fan, Bowang Zhang, Peisong Han,
Maolin Chen, *Member, IEEE*, and Wei Han, *Member, IEEE*

***Abstract*—The integration of renewable energy with electrolytic hydrogen production presents a promising pathway for reconciling generation-demand imbalances and reducing carbon-intensive hydrogen costs. However, existing power conversion systems suffer from critical limitations including excessive harmonic distortion, prohibitive output current ripple, and inadequate fault tolerance under high-current operation. This article proposes a novel virtual 48-pulse rectifier topology incorporating modular passive pulse-multiplication circuits (PPMCs) to address these challenges. The key innovation lies in deploying symmetric PPMC modules at the dc side of a dual six-pulse rectifier pair, which strategically synthesizes multilevel current waveforms through passive component interactions. This configuration achieves three key merits: Unprecedented power quality with input total harmonic distortion $<3\%$ and output ripple $<1.5\%$; cost-effective scalability requiring only few of additional passive components compared to baseline 12-pulse systems; and inherent fault tolerance via parallel redundancy, maintaining functionality during single-module failures. The effectiveness of the proposed rectifier in electrolytic hydrogen production is demonstrated through validation with a 1.2 kW experimental prototype.**

***Index Terms*—Electrolytic hydrogen production, power quality, renewable energy, three-phase.**

I. INTRODUCTION

CURRENTLY, researchers are increasingly focusing on addressing the issue of curtailed solar power and power restrictions [1]. The Integrated photovoltaic-energy storage-hydrogen production system has provided a new perspective for addressing the problem of abandoned light, holding significant importance in enabling on-site photovoltaic consumption and the efficient utilization of renewable energy through various channels [2], [3]. Scholars from diverse countries have extensively researched hydrogen energy storage coupled with renewable energy systems, proposing a range of solutions. These include adaptive neuro-fuzzy inference methods based on wind solar storage hydrogen systems [4], power management strategies based on state control [5], and online power regulation of wind-solar storage hydrogen coupled systems based on weight adjustment model predictive control [6].

Few studies have delved into the investigation of hydrogen production power supplies, which serve as critical components in the process. This oversight significantly hampers the broader adoption of hydrogen energy technologies. Fig. 1 is the schematic diagram of hydrogen production by electrolysis of water. In addition, Koponen et al. [7] studied the relationship between the current quality and Hydrogen production efficiency, where the mathematical relationship is shown in (1). The findings demonstrate that the hydrogen production rate f_{H2} of a single electrolyzer is directly proportional to the average current i_{cell}; and the presence of current ripples incurs additional losses in the electrolyzer. Consequently, it is imperative to utilize a power supply characterized by high amplitude and minimal ripple to ensure elevated hydrogen production and transmission efficiencies. In this regard, the 12-PR emerges as the optimal choice for a hydrogen production power source, offering significant benefits due to its simple circuit structure, high reliability, low cost, and enhanced overload capacity [8]. Nonetheless, the input current of the 12-PR contains a large number of 12k±1 harmonics, resulting in a total harmonic distortion (THD) of

---

Received 30 June 2025; revised 7 September 2025; accepted 8 October 2025. Date of publication 13 October 2025; date of current version 19 January 2026. This work was supported in part by Guangdong Basic and Applied Basic Research Fund under Grant 2025A1515012012 and in part by Brilliant Energy Science and Technology Lab (BEST Lab) at HKUST(GZ). Recommended for publication by Associate Editor M. Ordonez. *(Corresponding author: Wei Han.)*

Hanlei Tian, Jinliang Huang, Junyu Fan, and Bowang Zhang are with the Sustainable Energy and Environment Thrust, The Hong Kong University of Science and Technology (Guangzhou), Guangzhou 511453, China (e-mail: thledu@ieee.org; jhuang627@connect.hkust-gz.edu.cn; jfan822@connect.hkust-gz.edu.cn; bzhang794@connect.hkust-gz.edu.cn).

Guozhuang Liang is with the Electrical Engineering School of Hebei University of Science and Technology, Shijiazhuang 050091, China (e-mail: guozhuangliang@hebust.edu.cn).

Peisong Han is with the School of Electrical Engineering, Yanshan University, Qinhuangdao 066004, China (e-mail: hps@stumail.ysu.edu.cn).

Maolin Chen is with the College of Electrical Engineering, Sichuan University, Chengdu 610065, China (e-mail: chenml@alu.scu.edu.cn).

Wei Han is with the Sustainable Energy and Environment Thrust, The Hong Kong University of Science and Technology (Guangzhou), Guangzhou 511453, China, and also with the Department of Electronic and Computer Engineering, The Hong Kong University of Science and Technology, Hong Kong (e-mail: weihan@hkust-gz.edu.cn).

Color versions of one or more figures in this article are available at https://doi.org/10.1109/TPEL.2025.3620987.

Digital Object Identifier 10.1109/TPEL.2025.3620987

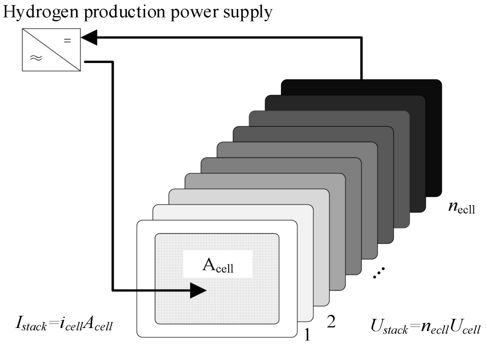

Fig. 1. Principle diagram of hydrogen production by electrolysis of water.

15.2%, which fails to comply with the harmonic standards prescribed by IEEE519. Furthermore, the considerable ripple in the output current detrimentally impacts the efficiency of hydrogen production

$$f_{H2} = \eta_F \frac{i_{\text{cell}} A_{\text{cell}}}{2 \times 9.6485 \times 104\ \text{C}\,\text{mol}^{-1}}. \tag{1}$$

In response to this, two principal approaches are employed, namely active and passive methods. Active methods involve the increasing use of pulsewidth modulation (PWM) rectifiers as front-end interfaces to reduce harmonic pollution in terrestrial applications, as studied in [9] and [10]. Nonetheless, compared to passive methods, PWM techniques do not offer advantages in terms of power capacity, cost, or efficiency, as thoroughly assessed in [11] and [12]. In this regard, many studies have attempted dc-side passive current modulation technology. The principle of this technology involves utilizing an enhanced tapped reactor to generate a square wave circulating current on the dc side. This approach not only compensates for grid-side harmonics but also effectively suppresses ripples on the dc side. In [13], [14], and [15], a dual auxiliary transformer is adopted to fulfill the above purpose. However, it is necessary to install two large capacitors on the dc side of the rectifier to establish a neutral point. In [16], [17], [18], [19], and [20], various passive pulse multiplication rectifiers, including single-phase full-wave rectifiers and tapped inter-phase bridge rectifiers, are utilized to enhance the current pulse count from 12 to 24, 12 to 36 and from 20 to 40. Further, Lian et al. [21] proposed a methodology that combines phase-shifting transformers with active reactors. This approach successfully facilitated the conversion from 12-pulse to 48-pulse configurations, while addressing the limitation of traditional reactors in achieving triple-pulse multiplication. While the aforementioned scheme effectively mitigates issues related to harmonics and ripples to some extent, it does not address the requirements for withstanding ultra-high currents essential for ensuring efficient hydrogen production. Consequently, these methods are not suitable for hydrogen production scenarios.

In view of this, this article proposes a novel symmetrical and parallel passive pulse-multiplication circuit (PPMC) architecture integrated with a 12-pulse rectifier, specifically designed for high-current-density hydrogen electrolyzers. The proposed topology achieves 48-pulse operation with minimal additional components, offering substantial improvements in both performance and reliability. Key innovations include a modular and symmetric design that simplifies manufacturing and enhances scalability, inherent fault tolerance allowing continuous operation during module failures, and superior power quality with input current THD below 3% and output current ripple under 1.5%. This article provides a cost-effective and robust power conversion solution tailored to the demanding requirements of electrolytic hydrogen production, addressing limitations of existing passive methods and offering new insights into high-efficiency rectifier design.

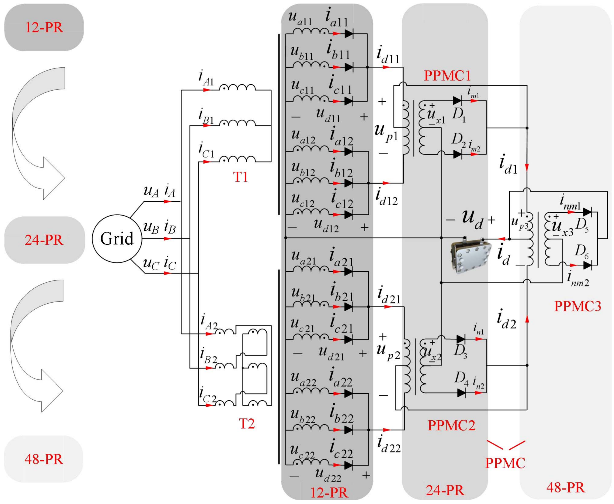

Fig. 2. Main circuit of the proposed hydrogen production rectifier.

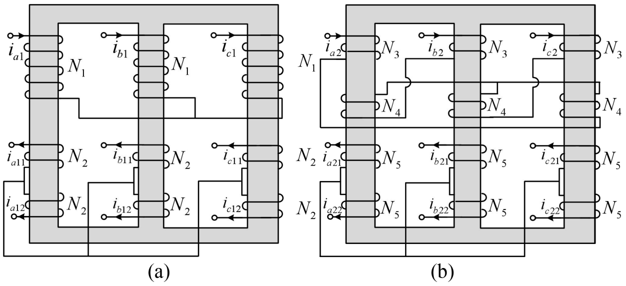

Fig. 3. Winding configuration of the double-star isolated transformer. (a) T1. (b) T2.

II. TOPOLOGY OF PROPOSED HYDROGEN PRODUCTION RECTIFIER

The proposed parallel topology consists of one 12-PR and three passive pulse-multiplication circuits (PPMC1, PPMC2, and PPMC3), as depicted in Fig. 2. Additionally, the PPMC comprises an injection transformer and two diodes.

The co-modulation structure is used to quadruple the pulse number of the 12-PR, ultimately achieving 48 pulses. Specifically, PPMC1 and PPMC2 respectively doubled the 6-PR to 12 pulses, and then PPMC3 doubled the 12 pulses to 24 pulses, ultimately forming 48 pulses. Additionally, Fig. 3 shows the winding configuration of the double-star isolated transformer, respectively. Similarly, Fig. 4 shows the winding configuration of the injection transformer, respectively.

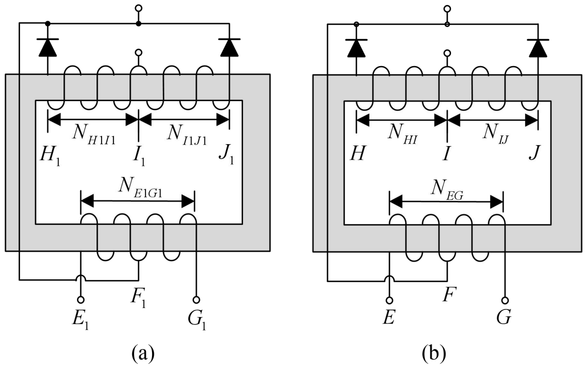

Fig. 4. Winding configuration of injection transformer. (a) PPMC1. (b) PPMC3.

III. ANALYSIS OF OPERATING CONDITIONS OF INJECTION TRANSFORMER

The turns-ratio derivation yields the optimal transformer turns ratio that ensures proper diode conduction and enables 48-pulse waveform synthesis. Before designing the injection transformer for PPMC, to simplify the analysis, the following assumptions and definitions are made as follows.

1) The proposed topology of hydrogen production rectifier is powered by a three-phase power grid, with no input voltage distortion and satisfying (2)
2) To achieve 45·phase shift, the structures of transformers $T1$ and $T2$ are shown in Fig. 2, with turn ratios of (3), respectively.
3) To facilitate further analysis, the turn ratio of the injection transformer is designed as N_{EG}:N_{HI}:N_{IJ} = 1:m:m

$$\begin{cases} u_A = U_m \sin(\omega t) \\ u_B = U_m \sin(\omega t - \frac{2\pi}{3}) \\ u_C = U_m \sin(\omega t + \frac{2\pi}{3}) \end{cases} \tag{2}$$

$$\begin{cases} \frac{N_2}{N_1} = \frac{N_5}{N_y} = k \\ \frac{N_3}{N_y} = k_2 = \frac{\sqrt{3}(\sqrt{6}-\sqrt{2})}{6} \\ \frac{N_4}{N_y} = k_3 = \frac{\sqrt{6}}{3} \end{cases} \tag{3}$$

where U_m is the amplitude of the phase voltage of the rectifier, and N_y is the effective turns of the primary winding, as expressed in

$$N_{\mathrm{y}} = \frac{N_3 + \frac{1}{2}N_4}{\cos\alpha} \tag{4}$$

where $\alpha = \pi/4$.

A. Injection Transformer PPMC1

The output voltage of the transformer $T1$ secondary side can be expressed as

$$\begin{cases} u_{a11} = kU_m \sin(\omega t), \quad u_{b11} = kU_m \sin(\omega t - \frac{2\pi}{3}) \\ u_{c11} = kU_m \sin(\omega t + \frac{2\pi}{3}), \quad u_{a12} = kU_m \sin(\omega t - \pi) \\ u_{b12} = kU_m \sin(\omega t + \frac{\pi}{3}), \quad u_{c12} = kU_m \sin(\omega t - \frac{\pi}{3}) \end{cases}. \tag{5}$$

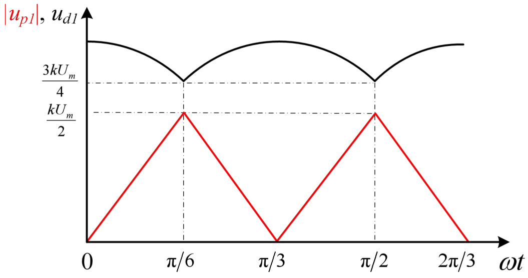

Fig. 5. Theoretical waveforms of $|u_{p1}|$, and u_{d1}.

When PPMC1 is inactive, the output voltage of THR1 and THR2 can be expressed as

$$u_{d11} = \max(u_{a11}, u_{b11}, u_{c11}), \quad u_{d12} = \max(u_{a12}, u_{b12}, u_{c12}). \tag{6}$$

The output voltage of PPMC1 is

$$u_{d1} = \frac{u_{d11} + u_{d12}}{2}. \tag{7}$$

The absolute value of PPMC1 primary winding voltage is

$$|u_{p1}| = |u_{d11} - u_{d12}|. \tag{8}$$

In accordance to (5)–(8) and Krichhoff's voltage law, u_{d11}, u_{d12}, u_{d1}, $|u_{p1}|$ are expressed as

$$u_{d11} = \begin{cases} kU_m \sin(\omega t + \frac{2\pi}{3}) & \omega t \in (0, \frac{\pi}{6}] \\ kU_m \sin(\omega t) & \omega t \in (\frac{\pi}{6}, \frac{5\pi}{6}] \\ kU_m \sin(\omega t - \frac{2\pi}{3}) & \omega t \in (\frac{5\pi}{6}, \frac{3\pi}{2}] \\ kU_m \sin(\omega t + \frac{2\pi}{3}) & \omega t \in (\frac{3\pi}{2}, 2\pi] \end{cases}$$

$$u_{d12} = \begin{cases} kU_m \sin(\omega t + \frac{\pi}{3}) & \omega t \in (0, \frac{\pi}{2}] \\ kU_m \sin(\omega t - \frac{\pi}{3}) & \omega t \in (\frac{\pi}{2}, \frac{7\pi}{6}] \\ kU_m \sin(\omega t - \pi) & \omega t \in (\frac{7\pi}{6}, \frac{11\pi}{6}] \\ kU_m \sin(\omega t + \frac{\pi}{3}) & \omega t \in (\frac{11\pi}{6}, 2\pi] \end{cases} \tag{9}$$

$$u_{d1} = \begin{cases} \frac{\sqrt{3}kU_m}{2} \sin(\omega t + \frac{\pi}{2}) \omega t \in (0, \frac{\pi}{6}] \\ \frac{\sqrt{3}kU_m}{2} \sin(\omega t + \frac{\pi}{6} - \frac{2n\pi}{6}) \omega t \in (\frac{2n+1}{6}\pi, \frac{2n+3}{6}\pi] \\ \frac{\sqrt{3}kU_m}{2} \sin(\omega t + \frac{\pi}{2}) \omega t \in (\frac{11\pi}{6}, 2\pi] \end{cases}$$

$$|u_{\mathrm{p1}}| = \begin{cases} kU_m \sin(\omega t) \omega t \in (0, \frac{\pi}{6}] \\ -kU_m \sin(\omega t - \frac{\pi}{3}) \omega t \in (\frac{\pi}{6}, \frac{\pi}{3}] \\ kU_m \sin(\omega t - \frac{\pi}{3}) \omega t \in (\frac{\pi}{3}, \frac{\pi}{2}] \\ kU_m \sin(\omega t + \frac{\pi}{3}) \omega t \in (\frac{\pi}{2}, \frac{2\pi}{3}] \end{cases}. \tag{10}$$

According to the structure of PPMC1 in the rectifier, the relationship between the absolute value of the voltage u_{p1} and the voltage u_{d1} determines the operating modes of PPMC, and the waveform is shown in Fig. 5.

In accordance to Fig. 5, when $\omega t = \pi/6$, u_{p1} and u_{d1} are both peak values. PPMC1 is operated properly, then

$$|u_{\mathrm{x1}}| = m_1 |u_{p1}| \geq u_{d1}. \tag{11}$$

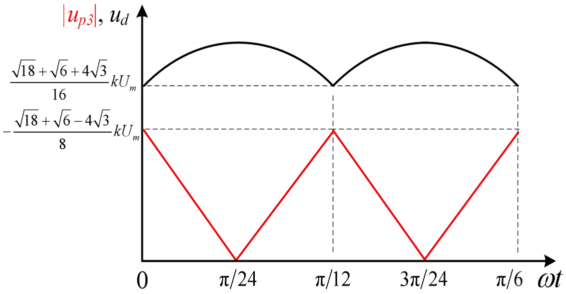

Fig. 6. Theoretical waveform of $|u_{p3}|$, and u_d.

Substituting (10) into (11), we have

$$m_1 \geq \left.\frac{u_{d1}}{|u_{p1}|}\right|_{\omega t=\frac{\pi}{6}} \geq 1.5. \tag{12}$$

Consequently, to guarantee the regular operation of PPMC1, the turn ratio must exceed 1.5. Similarly, the turn ratio for PPMC2 is also required to be greater than 1.5.

B. Injection Transformer PPMC3

To facilitate the analysis of PPMC3, decoupling analysis method is used, and PPMC1 and PPMC2 are set to operate at the optimal transformation ratio. Consequently, the output voltage is calculated as

$$\begin{gathered} u_{d1} = \begin{cases} \frac{\sqrt{3}}{2}kU_m\cos(\omega t) & \omega t \in (0, \frac{\pi}{12}] \\ \frac{\sqrt{3}}{2}kU_m\sin(\omega t+\frac{\pi}{3}) & \omega t \in (\frac{\pi}{12}, \frac{\pi}{4}] \\ \frac{\sqrt{3}}{2}kU_m\sin(\omega t+\frac{\pi}{6}) & \omega t \in (\frac{\pi}{4}, \frac{\pi}{3}] \end{cases} \\ u_{d2} = \begin{cases} \frac{\sqrt{3}}{2}kU_m\sin(\omega t+\frac{5\pi}{12}) & \omega t \in (0, \frac{\pi}{6}] \\ \frac{\sqrt{3}}{2}kU_m\sin(\omega t+\frac{3\pi}{12}) & \omega t \in (\frac{\pi}{6}, \frac{\pi}{3}] \end{cases}. \end{gathered} \tag{13}$$

In accordance to (7) and (8), similarly u_d and $|u_{p3}|$ are calculated following:

$$u_d = \begin{cases} \frac{\sqrt{3}}{4}kU_m[\cos(\omega t)+\sin(\omega t+\frac{5\pi}{12})] & \omega t \in (0, \frac{\pi}{12}] \\ \frac{\sqrt{3}}{4}kU_m[\sin(\omega t+\frac{\pi}{3})+\sin(\omega t+\frac{5\pi}{12})] & \omega t \in (\frac{\pi}{12}, \frac{\pi}{6}] \end{cases} \tag{14}$$

$$|u_{p3}| = \begin{cases} \frac{\sqrt{3}}{2}kU_m[\cos(\omega t)-\sin(\omega t+\frac{5\pi}{12})] & \omega t \in (0, \frac{\pi}{24}] \\ -\frac{\sqrt{3}}{2}kU_m[\cos(\omega t)-\sin(\omega t+\frac{5\pi}{12})] & \omega t \in (\frac{\pi}{24}, \frac{\pi}{12}] \\ -\frac{\sqrt{3}}{2}kU_m[\sin(\omega t+\frac{\pi}{3})-\sin(\omega t+\frac{5\pi}{12})] & \omega t \in (\frac{\pi}{12}, \frac{3\pi}{24}] \\ \frac{\sqrt{3}}{2}kU_m[\sin(\omega t+\frac{\pi}{3})-\sin(\omega t+\frac{5\pi}{12})] & \omega t \in (\frac{3\pi}{24}, \frac{\pi}{6}] \end{cases}. \tag{15}$$

In accordance to (14) and (15), the theoretical waveform of $|u_{p3}|$ and u_d is obtained, as shown in Fig. 6. From Fig. 6, while $wt = \pi/12$, u_{p3} and u_d are both peak values. Thus, PPMC3 is operated properly, then

$$|u_{x3}| = m_3\,|u_{p3}| \geq u_d \tag{16}$$

where u_{x3} is the second winding voltage of the PPMC3.

Substituting (14) and (15) into (16), thus we have (17). Consequently, to guarantee the normal operation of PPMC3, the turn ratio should be greater than 28.85. It should be noted that m_1 and m_3 differ markedly, owing to their different operating stages and the vastly different available excitation amplitudes

$$m_3 \geq \left.\frac{u_d}{|u_{p3}|}\right|_{\omega t=\frac{\pi}{12}} \geq 28.85. \tag{17}$$

IV. FAULT TOLERANCE ANALYSIS OF INJECTION TRANSFORMER

The flat region of the THD-versus-turns-ratio curve affords critical manufacturing tolerance for the transformer, underpinning high-volume manufacturability and fault tolerance. Consequently, this section will analyze the turn ratio design and and validate its fault tolerance characteristics of the injection transformer.

A. Optimal Turn Ratio of PPMC1

In accordance the Krichhoff‘s current law (KCL), the current i_{A1} can be expressed as

$$i_{A1} = k\left[\left(i_{a11}-\frac{1}{3}i_{d11}\right)-\left(i_{a12}-\frac{1}{3}i_{d12}\right)\right]. \tag{18}$$

According to the modal analysis, the current i_{d11} and i_{d12} can be expressed as

$$i_{d11} = \begin{cases} \frac{1}{2}I_d & \omega t \in (0,\theta_1], (\frac{\pi}{3}-\theta_1, \frac{\pi}{3}+\theta_1], (\frac{2\pi}{3}-\theta_1, \frac{2\pi}{3}] \\ 0 & \omega t \in (\theta_1, \frac{\pi}{3}-\theta_1] \\ \frac{2m_1}{2m_1+1}I_d & \omega t \in (\frac{\pi}{3}+\theta_1, \frac{2\pi}{3}-\theta_1] \end{cases} \tag{19}$$

$$i_{d12} = \begin{cases} \frac{1}{2}I_d & \omega t \in (0,\theta_1], (\frac{\pi}{3}-\theta_1, \frac{\pi}{3}+\theta_1], (\frac{2\pi}{3}-\theta_1, \frac{2\pi}{3}] \\ \frac{2m_1}{2m_1+1}I_d & \omega t \in (\theta_1, \frac{\pi}{3}-\theta_1] \\ 0 & \omega t \in (\frac{\pi}{3}+\theta_1, \frac{2\pi}{3}-\theta_1] \end{cases} \tag{20}$$

where θ_1 is the electrical angle when the working modes of PPMC1 changes for the first time in one period. The electrical angle meets

$$u_{d1}(\theta_1) = |u_{x1}(\theta_1)|\,. \tag{21}$$

Substituting (10) and (11) into (21), we have

$$\theta_1 = \arctan\left(\frac{\sqrt{3}}{2m_1}\right). \tag{22}$$

Meanwhile, the relationship between the current i_{a11}, i_{a12} and the current i_{d11}, i_{d12} can be respected by the following equations:

$$\begin{cases} i_{a11} = i_{d11}S_{a11}, & i_{b11} = i_{d11}S_{b11} \\ i_{c11} = i_{d11}S_{c11}, & i_{a12} = i_{d12}S_{a12} \\ i_{b12} = i_{d12}S_{b12}, & i_{c12} = i_{d12}S_{c12} \end{cases} \tag{23}$$

where $S_{a11}, S_{b11}, S_{c11}, S_{a12}, S_{b12,}$ and S_{c12} are the corresponding switching function, and S_{a11} is expressed by

$$S_{a11} = \begin{cases} 1 & \omega t \in [\frac{\pi}{6}, \frac{5\pi}{6}] \\ 0 & \text{Others} \end{cases}. \tag{24}$$

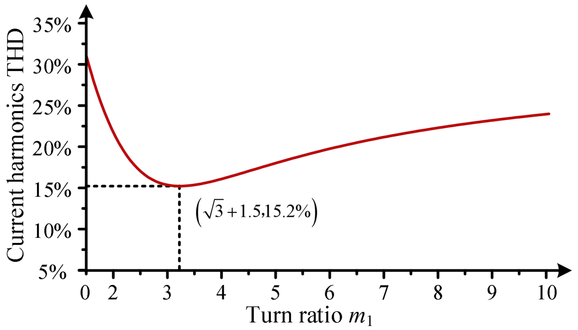

Fig. 7. Relation between THD and m_1.

Besides, the relationship between other switching functions and S_{a11} is obtained by

$$\begin{cases} S_{b21} = S_{a21}\angle -\frac{2\pi}{3}, \quad S_{c21} = S_{a21}\angle\frac{2\pi}{3} \\ S_{a22} = S_{a21}\angle -\pi, \quad S_{b22} = S_{b21}\angle -\pi \\ S_{c22} = S_{c21}\angle -\pi \end{cases}. \tag{25}$$

In accordance to (18), the input current i_{A1} is expressed by

$$i_{A1} = k\begin{cases} 0\omega t \in (0,\theta_1] \;, \frac{2m_1}{3(2m_1+1)} I_d\omega t \in (\theta_1, \frac{\pi}{3}-\theta_1] \\ \frac{1}{2} I_d\omega t \in (\frac{\pi}{3}-\theta_1, \frac{\pi}{3}+\theta_1], \; \frac{4m_1}{3(2m_1+1)} I_d\omega t \in (\frac{\pi}{3}+\theta_1, \frac{\pi}{2}] \end{cases}. \tag{26}$$

Furthermore, in accordance to (26), the THD of the current i_{A1} can be obtained as

$$\mathrm{THD}_{iA1} = \frac{\sqrt{I_{A1}^2 - I_1^2}}{I_1} \tag{27}$$

where I_{A1} and I_1 are the RMS value and the fundamental component of $iA1$, respectively. Both quantities are computed from (26) in MATLAB.

Subsequently, the relation between the current i_{A1} and the turn ratio m_1 is illustrated in Fig. 7 via MATLAB. From Fig. 7, when $m_1 = \sqrt{3} + 1.5$, the THD reaches its minimum value of 15.2%, and meets

$$\theta_1 = \arctan\left(\frac{\sqrt{3}}{2m_1}\right) = \frac{\pi}{12}. \tag{28}$$

Due to the proposed structure's good symmetry, the same derivation can also be applied to i_{A2}; however, further details will not be elaborated here. Fig. 7 illustrates that the trend around the optimal turn ratio is relatively flat, providing a substantial margin for fault tolerance in mass production. Furthermore, the fault tolerance results of the injection transformer will be discussed in the verification section.

B. Design and Analysis of PPMC3

In accordance the KCL, the current i_A can be expressed as

$$i_A = i_{A1} + i_{A2} \tag{29}$$

where the current i_{A1} and i_{A2} can be calculated by (26) and (30), respectively.

$$i_{A2} = k(k_2 i_{a21} - k_3 i_{c21} + \frac{i_{d21}}{6} - (k_2 i_{a22} - k_3 i_{c22} + \frac{i_{d22}}{6})). \tag{30}$$

According to the modal analysis, the current i_{d1} and i_{d1} satisfies (31) within one cycle

$$i_{d1} = \begin{cases} \frac{2m_3}{2m_3+1} I_d & \omega t \in (0, \theta_3] \\ \frac{1}{2} I_d & \omega t \in (\theta_3, \frac{\pi}{12}-\theta_3] \\ 0 & \omega t \in (\frac{\pi}{12}-\theta_3, \frac{\pi}{12}+\theta_3] \\ \frac{1}{2} I_d & \omega t \in (\frac{\pi}{12}+\theta_3, \frac{\pi}{6}-\theta_3] \\ \frac{2m_3}{2m_3+1} I_d & \omega t \in (\frac{\pi}{6}-\theta_3, \frac{\pi}{6}] \end{cases},$$

$$i_{d2} = \begin{cases} 0 & \omega t \in (0,\theta_3] \\ \frac{1}{2} I_d & \omega t \in (\theta_3, \frac{\pi}{12}-\theta_3] \\ \frac{2m_3}{2m_3+1} I_d & \omega t \in (\frac{\pi}{12}-\theta_3, \frac{\pi}{12}+\theta_3] \\ \frac{1}{2} I_d & \omega t \in (\frac{\pi}{12}+\theta_3, \frac{\pi}{6}-\theta_3] \\ 0 & \omega t \in (\frac{\pi}{6}-\theta_3, \frac{\pi}{6}] \end{cases} \tag{31}$$

where θ_3 is the angle at which PPMC3 undergoes its first mode transition within a cycle, and satisfies

$$u_d(\theta_3) = |u_x(\theta_3)|. \tag{32}$$

Similarly, the current $i_{d11}, i_{d12}, i_{d21}$ and i_{d22} are expressed by (A1) and (A2), the relationship between the current i_{a21}, i_{a22}, i_{c21}, i_{c22} and the current i_{d21}, i_{d22} is expressed by (35)

$$\begin{cases} i_{a21} = i_{d21}\mathrm{S}_{a21}, \quad i_{b21} = i_{d21}\mathrm{S}_{b21} \\ i_{c21} = i_{d21}\mathrm{S}_{c21}, \quad i_{a22} = i_{d22}\mathrm{S}_{a22} \\ i_{b22} = i_{d22}\mathrm{S}_{b22}, \quad i_{c22} = i_{d22}\mathrm{S}_{c22} \end{cases}. \tag{33}$$

For instance, the switching function of S_{a11} is

$$S_{a21} = \begin{cases} 1\omega t \in [0, \frac{7\pi}{12}], (\frac{23\pi}{12}, 2\pi] \\ 0\text{others} \end{cases}. \tag{34}$$

Subsequently, the relationship between other switching functions can be expressed as

$$\begin{cases} S_{b21} = S_{a21}\angle -\frac{2\pi}{3}, \quad S_{c21} = S_{a21}\angle\frac{2\pi}{3} \\ S_{a22} = S_{a21}\angle -\pi, \quad S_{b22} = S_{b21}\angle -\pi \\ S_{c22} = S_{c21}\angle -\pi \end{cases}. \tag{35}$$

Combining (12), (17), (18), (31), and (A1), the current i_{A1} can be obtained as (A3). Similarly, combining (30), (31), and (32)–(35) and (A2), the current i_{A2} can be obtained. Due to symmetry, only $[0, \frac{\pi}{2}]$ is analyzed. Then, combining (29) and (38), we have

$$i_A = k\begin{cases} 0\omega t \in (0,\theta_3] \\ k_2 \frac{1}{4} I_d\omega t \in (\theta_3, \frac{\pi}{12}-\theta_3] \\ k_2 \frac{m_3}{2m_3+1} I_d\omega t \in (\frac{\pi}{12}-\theta_3, \frac{\pi}{12}+\theta_3] \\ \frac{\sqrt{3}}{12} I_d + k_2 \frac{1}{4} I_d\omega t \in (\frac{\pi}{12}+\theta_3, \frac{\pi}{6}-\theta_3] \\ \frac{\sqrt{3}}{3} \frac{m_3}{2m_3+1} I_d\omega t \in (\frac{\pi}{6}-\theta_3, \frac{\pi}{6}+\theta_3] \end{cases},$$

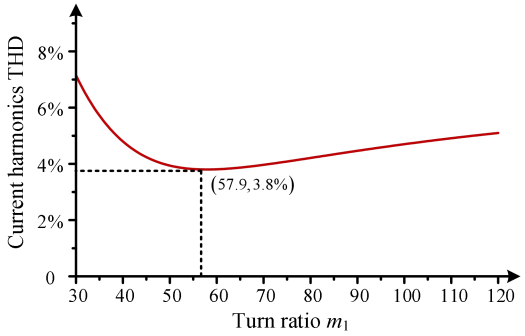

Fig. 8. Relation between THD and m_3.

$$k\begin{cases}\frac{\sqrt{3}}{12}I_d+(\frac{\sqrt{3}}{24}I_d+k_2\frac{\sqrt{3}}{4}I_d)\omega t\in(\frac{\pi}{6}+\theta_3,\frac{\pi}{4}-\theta_3]\\(\sqrt{3}k_2+\frac{\sqrt{3}}{6})\frac{m_3}{2m_3+1}I_d\omega t\in(\frac{\pi}{4}-\theta_3,\frac{\pi}{4}+\theta_3]\\\frac{1}{4}I_d+(\frac{\sqrt{3}}{24}I_d+k_2\frac{\sqrt{3}}{4}I_d)\omega t\in(\frac{\pi}{4}+\theta_3,\frac{\pi}{3}-\theta_3]\\\frac{m_3}{2m_3+1}I_d\omega t\in(\frac{\pi}{3}-\theta_3,\frac{\pi}{3}+\theta_3]\\\frac{1}{4}I_d+(k_2\frac{1}{4}I_d+k_3\frac{1}{4}I_d)\omega t\in(\frac{\pi}{3}+\theta_3,\frac{5\pi}{12}-\theta_3]\\(k_2+k_3)\frac{m_3}{2m_3+1}I_d\omega t\in(\frac{5\pi}{12}-\theta_3,\frac{5\pi}{12}+\theta_3]\\\frac{\sqrt{3}}{6}I_d+(k_2\frac{1}{4}I_d+k_3\frac{1}{4}I_d)\omega t\in(\frac{5\pi}{12}+\theta_3,\frac{\pi}{2}-\theta_3]\\\frac{\sqrt{3}}{3}\frac{2m_3}{2m_3+1}I_d\omega t\in(\frac{\pi}{2}-\theta_3,\frac{\pi}{2}]\end{cases}. \tag{36}$$

Similarly, the relation between the current i_A and the turn ratio m_3 be shown in Fig. 8 via MATLAB. From Fig. 8, when $m_3 = 57.9$, the THD reaches its minimum value of 3.8%. Meanwhile, the flat trend also appears in the design of injected transformer PDCC3.

V. PERFORMANCE ANALYSIS OF SYSTEM

The cost of injecting transformers, as the core component of the proposed rectifier, is particularly significant. Consequently, Consequently, the capacity of the injection transformers is analyzed in this section.

A. Capacity Analysis of PPMC3

Under the optimal turn ratio, the input voltage of PPMC3 u_p is expressed by

$$u_{p3}=k\begin{cases}\frac{\sqrt{3}}{2m_3+1}U_m\cos(x) & \omega t\in(0,\frac{\pi}{48}]\\\frac{\sqrt{3}}{2}U_m\left(\cos(x)-\sin\left(x+\frac{5\pi}{12}\right)\right) & \omega t\in(\frac{\pi}{48},\frac{3\pi}{48}]\\-\frac{\sqrt{3}}{2m_3+1}U_m\sin\left(x+\frac{5\pi}{12}\right) & \omega t\in(\frac{3\pi}{48},\frac{5\pi}{48}]\\\frac{\sqrt{3}}{2}U_m\left(\sin\left(x+\frac{\pi}{3}\right)-\sin\left(x+\frac{5\pi}{12}\right)\right) & \omega t\in(\frac{5\pi}{48},\frac{7\pi}{48}]\\\frac{\sqrt{3}}{2m_3+1}U_m\sin\left(x+\frac{\pi}{3}\right) & \omega t\in(\frac{7\pi}{48},\frac{\pi}{6}]\end{cases}. \tag{37}$$

According to (37), the mean square value (RMS) of the voltage u_p is obtained by

$$U_{p3\_\mathrm{rms}}=\sqrt{\frac{1}{2\pi}\int_0^{2\pi}(u_{p3})^2d(\omega t)}=0.014U_d. \tag{38}$$

Referring to the structure of PPMC3, the RMS of the voltage across the winding can be obtained as (39). Similarly, the RMS of the current I_{d1} is obtained based on (31)

$$\begin{cases}U_{EF\_\mathrm{rms}}=\frac{1}{2}U_{p3\_\mathrm{rms}}=0.007U_d \quad U_{FG\_\mathrm{rms}}\\\quad=\frac{1}{2}U_{p3\_\mathrm{rms}}=0.007U_d\\U_{HI\_\mathrm{rms}}=m_3U_{p3\_\mathrm{rms}}=0.811U_d \quad U_{IJ\_\mathrm{rms}}\\\quad=m_3U_{p3\_\mathrm{rms}}=0.811U_d\end{cases} \tag{39}$$

$$I_{d1\_\mathrm{rms}}=\sqrt{\frac{1}{2\pi}\int_0^{2\pi}(i_{d1})^2d(\omega t)}=0.609I_d. \tag{40}$$

Additionally, the current flowing through diode $D5$ can be expressed as (41). Its RMS can be obtained from (42).

$$i_{nm1}=\begin{cases}\frac{1}{2m_3+1}I_d & \omega t\in(0,\frac{\pi}{48}]\\0 & \omega t\in(\frac{\pi}{48},\frac{7\pi}{48}]\\\frac{1}{2m_3+1}I_d & \omega t\in(\frac{7\pi}{48},\frac{\pi}{6}]\end{cases} \tag{41}$$

$$I_{nm1\_\mathrm{rms}}=\sqrt{\frac{1}{2\pi}\int_0^{2\pi}(i_{nm1})^2d(\omega t)}=0.004I_d. \tag{42}$$

Combining the above equations, the capacity of PPMC3 can be obtained by

$$\begin{aligned}S_{\mathrm{PPDC3}}&=\frac{1}{2}(U_{EF\_\mathrm{rms}}I_{d1\_\mathrm{rms}}+U_{FG\_\mathrm{rms}}I_{d2\_\mathrm{rms}}\\&\quad+U_{HI\_\mathrm{rms}}I_{nm1\_\mathrm{rms}}+U_{IJ\_\mathrm{rms}}I_{nm2\_\mathrm{rms}})\\&=0.75\%P_o.\end{aligned} \tag{43}$$

B. Capacity Analysis of PPMC1

The input voltage of PPMC1 u_{p1} is expressed by

$$u_{p1}=k\begin{cases}-U_m\sin(x) & \omega t\in(0,\frac{\pi}{12}]\\-\frac{2}{(2\sqrt{3}+4)}U_m\sin\left(x+\frac{\pi}{3}\right) & \omega t\in(\frac{\pi}{12},\frac{\pi}{4}]\\U_m\sin\left(x-\frac{\pi}{3}\right) & \omega t\in(\frac{\pi}{4},\frac{5\pi}{12}]\\\frac{2}{(2\sqrt{3}+4)}U_m\sin(x) & \omega t\in(\frac{5\pi}{12},\frac{7\pi}{12}]\\U_m\sin\left(x+\frac{\pi}{3}\right) & \omega t\in(\frac{7\pi}{12},\frac{2\pi}{3}]\end{cases}. \tag{44}$$

Combining (40) and (44), we have

$$U_{p1\_\mathrm{rms}}=\sqrt{\frac{1}{2\pi}\int_0^{2\pi}u^2{}_{p1}d(\omega t)}=0.251U_d. \tag{45}$$

Referring to the structure of PPMC1, the RMS of the voltage across the winding can be obtained as (46). Similarly, the RMS of the current i_{d11} is obtained based on (47)

$$\begin{cases}U_{E1F1\_\mathrm{rms}}=\frac{1}{2}U_{p1\_\mathrm{rms}}=0.126U_d \quad U_{F1G1\_\mathrm{rms}}\\\quad=\frac{1}{2}U_{p1\_\mathrm{rms}}=0.126U_d\\U_{H1I1\_\mathrm{rms}}=m_1U_{p1\_\mathrm{rms}}=0.811U_d \quad u_{I1J1\_\mathrm{rms}}\\\quad=m_1U_{p1\_\mathrm{rms}}=0.811U_d\end{cases} \tag{46}$$

$$I_{d11\_\mathrm{rms}}=\sqrt{\frac{1}{2\pi}\int_0^{2\pi}(i_{d11})^2d(\omega t)}=0.340I_d. \tag{47}$$

TABLE I
COMPARISON RESULTS BETWEEN PROPOSED METHOD AND SIMILAR WORKS

Indicators		**Conventional 48-pulse method**	**Tian et al [17]**	**Wang et al. [22]**	**Li et al. [23]**	**Akther et al. [24]**	**Chen et al. [25]**	**Proposed method**
THD of input current		1.5%-5%	3.2%	3.81%	<3.91%	4.75%	3.51%	2.88%
AC and DC side is isolated or not		Yes	Yes	No	Yes	Yes	No	Yes
Efficiency of rectifier		≈95%	98.1	97.3%	-	-	98.3%	97.6%
Stability of output voltage		/	Good	Good	Bad	Good	Good	Good
Harmonic suppression method		/	Current injection	Current injection	Voltage injection	Current injection	Current injection	Current injection
Number of components	Output side capacitors	0	0	0	3	0	0	0
	Output side diodes	48 (Main)	12 (Main) 6 (Parallel)	12 (Main) 3 (Series) 4(Parallel)	12 (Main) 6 (Parallel)	24 (Main) 2 (Series)	12 (Main) 2 (Series) 4 (Parallel)	12 (Main) 6 (Parallel)
	Output side MOSFET	0	0	3 (Series)	2 (Parallel)	0	0	0
Zero-sequence blocking transformers		0	0	1	0	0	2	0
Phase-shifting transformer connection type		Delta-wye-wye or Star-delta and et al	Delta-wye-wye	Delta-connected autotransformer	Delta-zigzag-wye-zigzag	Wye-zigzag-zigzag-wye-zigzag	Polygon-connected autotransformer	Delta-wye-wye
Overall magnetic ratings		>420%	127%	-	-	-	31.575% (Autotransformer)	129.7%
Application scenarios		Low, medium and high voltage, high power	Electrolysis, and other low voltage, high current	Medium and high voltage, low current, Medium power	Low and Medium voltage/ current, high power	Medium and high voltage, low current, high power	Medium and high voltage, low current, Medium power	Electrolysis, and other low voltage, high current

Note: Ref. [21] for calculating voltage stability. / indicates that the method has not been adopted. - means the parameter does not exist.

The current flowing through diode $D1$ I_{D1} can be expressed as (48). Furthermore, its RMS can be obtained from (49)

$$i_{m1} = \begin{cases} 0 & \omega t \in (0, \frac{21\pi}{48}] \\ \frac{1}{4\sqrt{3}+8} I_d & \omega t \in (\frac{21\pi}{48}, \frac{23\pi}{48}] \\ \frac{1}{2\sqrt{3}+4} \frac{2m_3}{2m_3+1} I_d & \omega t \in (\frac{23\pi}{48}, \frac{25\pi}{48}] \\ \frac{1}{4\sqrt{3}+8} I_d & \omega t \in (\frac{25\pi}{48}, \frac{27\pi}{48}] \\ 0 & \omega t \in (\frac{27\pi}{48}, \frac{2\pi}{3}] \end{cases} \tag{48}$$

$$I_{m1\_\mathrm{rms}} = \sqrt{\frac{1}{2\pi} \int_0^{2\pi} (i_{m1})^2 d(\omega t)} = 0.041 I_d. \tag{49}$$

Combining the above equations, the capacity of PPMC1&PPMC2 can be obtained by

$$\begin{aligned} S_{\mathrm{PPDC1}} = S_{\mathrm{PPDC2}} &= \frac{1}{2}(U_{E1F1\_\mathrm{rms}} I_{d11\_\mathrm{rms}} \\ &\quad + U_{F1G1\_\mathrm{rms}} I_{d12\_\mathrm{rms}} \\ &\quad + U_{H1I1\_\mathrm{rms}} I_{m1\_\mathrm{rms}} + U_{I1J1\_\mathrm{rms}} I_{m2\_\mathrm{rms}}) \\ &= 7.61\% P_o. \end{aligned} \tag{50}$$

Based on the aforementioned analysis, the proposed method maintains a kVA rating approximately equivalent to that of the rectifier without PPMC. However, it significantly reduces the harmonics and ripple compared to the rectifier without PPMC.

Besides, based on the RMS voltage and current derivations in (39)–(50), we formulate a scalable loss-and-thermal modeling framework for higher power ratings (50–250 kW, 1–2 kA). In this framework, the analytical waveforms provide the RMS and average currents of each winding and diode, from which the copper loss is evaluated as in (51). The RMS voltages then determine the magnetic flux density and, together with the selected core material characteristics, enable estimation of the core loss. Diode conduction loss is computed using (52). Although the present work does not include experimental measurements at 50–250 kW, the modeling procedure follows directly from closed-form expressions and is therefore applicable to larger-scale implementations. Moreover, because the reported total magnetic rating (129.7%) is a topology-normalized metric, this percentage remains essentially invariant under power scaling, whereas the absolute magnetic kVA increases approximately linearly with output power

$$P_{\mathrm{cu}} = \Sigma I_{\mathrm{rms}}^2 \cdot R_T \tag{51}$$

$$P_{\mathrm{d}} \approx V_f \cdot I_{\mathrm{avg}} + r_d \cdot I_{\mathrm{rms}}^2 \tag{52}$$

where R_T is the equivalent resistance of winding, V_f is the equivalent conduction voltage drop of diode, and r_d is equivalent dynamic resistance of diode.

VI. COMPARATIVE ANALYSIS

To illustrate the strengths and weaknesses of the proposed method, Table I gives a comparison with similar works discussed in [22], [21], [23], [24] and [25].

From the perspective of the cost, the total cost of the multipulse rectifier is primarily determined by the capacity of the magnetic devices, creating a direct proportional relationship between the total cost and the capacity of these devices. Compared to the conventional 48-pulse method, the PPMC structures proposed in this article, as given in Table I, replace the need for multiple phase-shifting transformers, significantly reducing the total magnetic ratings. Compared to [24] and [25], the proposed method has a higher total magnetic rating, because of the autotransformer employed in [24]. The autotransformer-based solutions, which lack galvanic isolation and require two additional zero-sequence blocking transformers, are unsuitable for low-voltage, high-current hydrogen production applications where safety, equipment protection, and electrolysis efficiency are critical. Also, the rectifier provides a scenario (200 V/5000 A, 1 MW), as shown in Table II. While comparing the total costs of $M1$, $M2$ and the proposed method M3 offers savings of

TABLE II
COST OF DIFFERENT RECTIFIERS

Method (200V/5000A, 1MW)	M1	M2	M3
Transformer	\$30 000	\$20 000	\$20 600
Power switching/diode device	\$7200	\$17 000	\$3900
Capacitor and inductor	\$1100	\$6000	\$1100
Control, sensor, and driver	\$1500	\$5000	\$375
Total	\$39 800	\$48 000	\$25 975

Note: M1 is conventional 48-pulse rectifier achieved by cascading 12-pulse rectifiers. M2 is PWM+6-pulse rectifier reported in [4]. M3 is proposed method.

approximately 53% and 85%, respectively. It's important to note that these costs will increase as the nominal power rating rises. Additionally, while the base failure rate of thyristors/diodes is less than 22 failure in time (FIT), the insulated gate bipolar transistor's failure rate is 100 FIT, as reported in [4].

From the perspective of stability, the use of large capacitors in [23] not only increases capacitor losses but also reduces the lifespan of the rectifier. Meanwhile, it is based on voltage injection, and requires three large inductors to be connected in series on the input side of the rectifier to achieve harmonic suppression. These inductors not only reduce the displacement factor of the rectifier but also soften its output characteristics. In contrast, the proposed method in this article avoids using capacitors as components in the injection circuit. In addition, the asymmetric design proposed in [17] demonstrates substantially greater sensitivity around the optimal turns ratio than our proposed design, resulting in inferior THD and ripple performance.

From the design complexity, the complexity of the rectifier structure is primarily determined by the injection circuit's complexity. To achieve the limitation of doubling the pulse by three times, Wang et al. [22] and Li et al. [23] used switches in the injection circuit, which not only increased the complexity of control, but also significantly increased the cost of using detection units. To match the auxiliary converter ACIU, Tian et al. [17] mandates precise trimming of the main transformer secondary turns ratio (k_2:k_1 $= 0.983$:1), significantly raising manufacturing complexity.

From the perspective of application scenario, the electrolyzer systems operate in a low-voltage, high-current regime, and the hydrogen production rate is approximately proportional to the stack current. Consequently, inserting power semiconductors directly in series with the load is impractical at these currents due to excessive conduction loss and thermal stress. Compared with the approaches in [22], [24], and [25], the proposed parallel topology is better suited to this regime, offering lower conduction losses and superior high-current capability.

VII. RESULTS AND DISCUSSION

Fig. 9 presents the 1.2-kW proof-of-concept prototype. During testing, a 3 Ω series resistor is inserted with the electrolyzer to divide the dc-link voltage. Also, the detailed prototype parameters are given in Table III. All hydrogen-production comparison experiments were conducted on the same electrolyzer with the same balance-of-plant. The experimental settings match those used in the simulations.

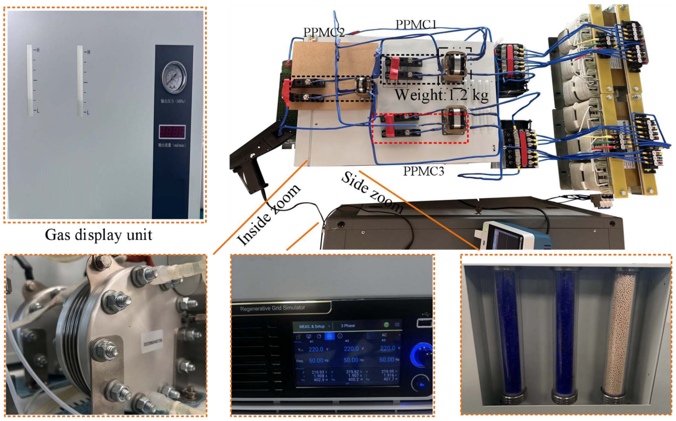

Electrolytic cell Power grid simulator Drying unit

Fig. 9. Experimental setup.

TABLE III
EXPERIMENTAL PARAMETERS

Description	Value	Description	Value
Input voltage	380 V	Turn ratio of PPMC1	√3+1.5
Bus frequency	50 Hz	Turn ratio of PPMC3	57.9
Voltage division R	3 Ω	Turn ratio of T	380:60:√3*60
DC voltage (Mean)	82.3 V	Diode	MDS60A, MDQ60A

Note: T is the phase-shifting transformer, R is the resistance.

First, the analysis of power quality is presented as follows. As presented in Fig. 10(a), the simulation results for the input current demonstrate 48 steps within one cycle, and the main low-order currents are largely eliminated, indicating effective suppression of input current harmonics by the PPMC. To accommodate electrolyzers of different powers, Fig. 10(b) and (c) shows full-load and dynamic conditions, respectively. It is observed that the THD is 2.88% under half-load and 2.96% under dynamic conditions. In comparison, as shown in Fig. 10(d), the proposed method significantly outperforms the rectifier without PPMC, which exhibits a THD of 13%. Taking into account the filtering characteristics of the leakage inductance from the phase-shifting transformer, the measured value of the input current's THD at 2.88% is marginally lower than the simulated value of 3.36%, as presented in Fig. 10(e). Fig. 10(f) shows the input and output current waveforms of the proposed rectifier operating at 100 kW. It can be seen that its performance is still excellent, as evidenced by the clear 48-step.

Second, the proposed method eliminates the need for filtering inductance, significantly attenuating the harmonics and ripple of the current, which makes it particularly suitable for hydrogen production applications. Consequently, the waveform of the PPMC is presented here. The simulation and experimental results of the current i_{m1} flowing through diode D_1 of PPMC1 are shown in Fig. 11(a) and (b), and the current presents three-level dc current within one cycle due to the modulation by PPMC1 and PPMC3. Additionally, the simulation and experimental results of

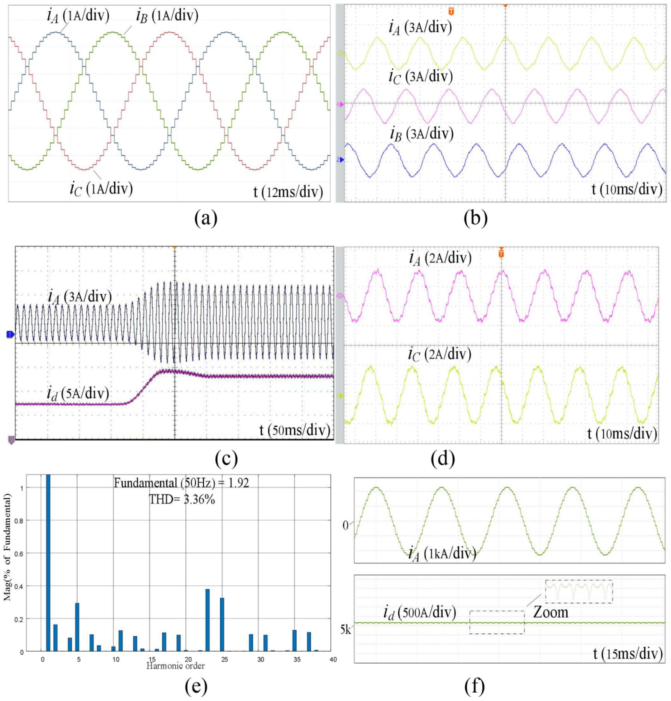

Fig. 10. Results of performance testing. (a) Simulation result of input current without leakage inductance. (b) Experimental result of input current of proposed method under full load. (c) Dynamic testing. (d) Experimental result of rectifier without PPMC under full load. (e) Harmonic order of proposed method. (f) High power simulation testing.

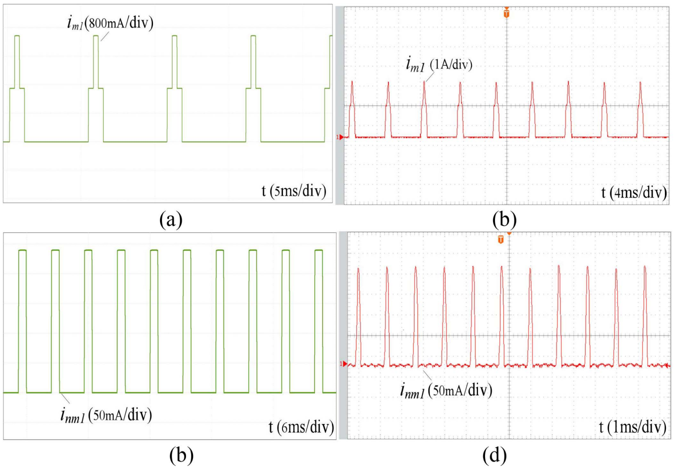

Fig. 11. Results of performance testing. (a) Simulation result of current i_{m1} flowing through diode D_1 of PPMC1. (b) Experimental result of current i_{m1} flowing through diode D_1 of PPMC1. (c) Simulation result of current i_{nm1} flowing through diode D_5 of PPMC3. (d) Experimental result of current i_{nm1} flowing through diode D_5 of PPMC3.

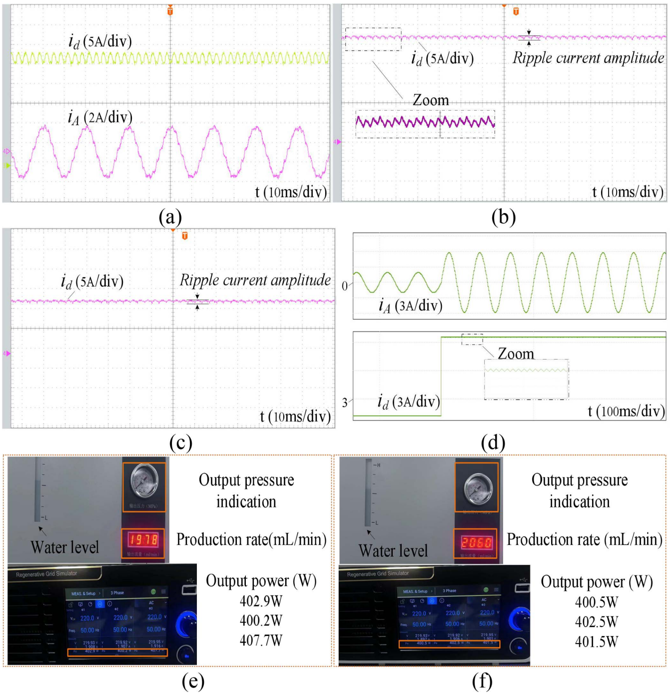

Fig. 12. Results of performance testing. (a) Output current of rectifier without PPMC under full load. (b) Output current of proposed method under full load. (c) Output current of proposed method under half load. (d) Simulation results of dynamic testing. (e) Display of H_2 meter of rectifier without PPMC. (f) Display of H_2 meter of proposed method.

the current flowing through diode D_5 of PPMC3 i_{nm1} are shown in Fig. 11(c) and (d). From the simulation and experimental results, it is a square-wave current with a frequency of 600 Hz. Owing to the filtering effect of transformer leakage inductance, the measured current i_{m1} and i_{nm1} are smoother than the simulation results. Additionally, the peak of the measured current i_{m1} and i_{nm1} are 3.1 A and 230 mA, respectively. It means that the power rating of PPMC is much smaller.

Thirdly, discrepancies between the mean value and RMS value contribute to additional losses in the electrolyzer. Thus, the improvement of hydrogen production efficiency is attributed to the reduction of losses in the electrolyzer. Compared to the output current of the rectifier without PPMC as illustrated in Fig. 12(a), the measured maximum output current ripple is decreased from 3.87 to 0.37 A, as shown Fig. 12(b). Moreover, the dc crest-factor is decreased from 1.15 to 1.01 under full load. The elimination of current peaks ensures that virtually all of the input power is utilized for the electrochemical water-splitting reaction, rather than being dissipated as additional losses induced by current ripple. Fig. 12(c) shows the half load condition, and the MSV and the RMS of the output current are 13.013 and 13.015 A, respectively. Additionally, it is worth noting that the proposed method still maintains a low ripple rate of only 1.46% from 30% to 100% load, as presented in Fig. 12(d). As shown in Figs. 12(e) and 10(f), the production rate of the rectifier without PPMC (1978 mL/min) and the proposed method (2060 mL/min) is different under the same parameter, and the comparison results are summarized in Table IV. With proposed PPMC, the dc output-current ripple is reduced by 90.4%, which yields a 4.2% reduction in specific energy consumption (kWh·Nm^{-3}) and a 4.1% increase in the hydrogen production rate. Consequently, the proposed method is demonstrably more effective and appropriate for scenarios involving hydrogen production.

TABLE IV
COMPARISON RESULTS WITH/WITHOUT PPMC

Condition	Input current THD	Output current ripple	hydrogen production rate	Energy consumption per unit (kWh/Nm^3)
Without PPMC	13%	3.87 A	1978 mL/min	4.8
With PPMC	2.88%	0.37 A	2060 mL/min	4.6

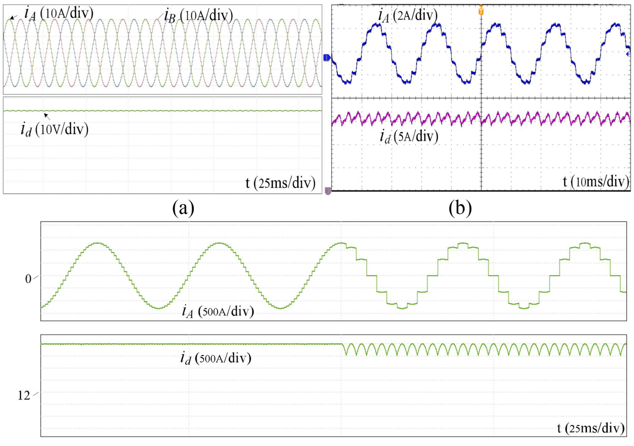

(a) (b)

(c)

Fig. 13. Results of performance testing. (a) Simulation result of output current and input current considering fault tolerance of PPMC-10%. (b) Fault tolerance for only PPMC$_1$ operation. (c) Instantaneous simulation testing for only PPMC$_1$ operation.

Finally, further assessments of performance, including fault tolerance, have been conducted. Fig. 13(a) presents the input and output currents, respectively, accounting for error margins of -10% in the PPMC configuration. The simulation results indicate that the harmonics in the input current remains below 3.5%, respectively. Fig. 13(b) shows the input-current and output-current waveforms with PPMC$_2$ and PPMC$_3$ disabled. Fig. 13(c) shows the instantaneous simulation result of only PPMC$_1$ operation. With a symmetrical parallel circuit design, the proposed method maintains stable operation and presents waveforms comparable to those of a 12-pulse rectifier, consistent with the topology analysis in Section II. Practically, the THD is expected to reduce further due to the presence of leakage inductance. Fig. 14 presents the efficiency curve, which peaks at 97.6% near 1.1 kW. PPMC adopts partial-power processing, routing the bulk power through a low-loss direct path and thereby avoiding the conduction, circulating-current/commutation, and magnetic/copper losses inherent to multistage phase-shifted, multibridge 48-pulse rectifiers, which improves efficiency.

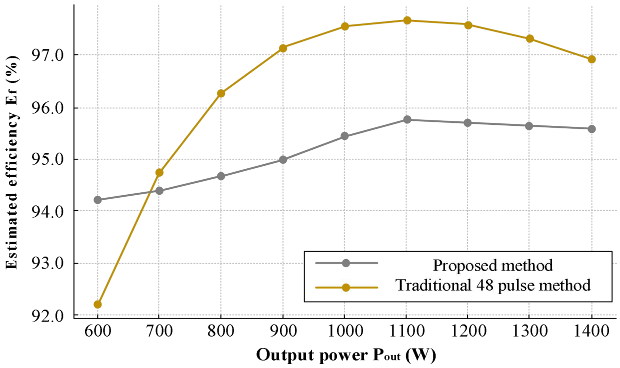

Fig. 14. Efficiency curves at different output powers.

VIII. CONCLUSION

A novel type of rectifier specifically designed for low voltage and high current applications, providing new ideas for electrolytic hydrogen production. In this research, the operation requirements, input current, output current, and kVA rating are analyzed in detail. The simulation and experimental results are carried out to confirm the feasibility of the theoretical analysis. The results showed that the ripple and harmonic were effectively controlled below 1.5% and 3%, respectively. Finally, the fault tolerance characteristics facilitate mass production, and the lower costs make it feasible to expand power capacity seamlessly.

APPENDIX

$$i_{d11}=\begin{cases}\frac{m_3}{2m_3+1}I_d & \omega t\in(0,\theta_3]\\ \frac{1}{4}I_d & \omega t\in(\theta_3,\frac{\pi}{12}-\theta_3]\\ 0 & \omega t\in(\frac{\pi}{12}-\theta_3,\frac{\pi}{4}+\theta_3]\\ \frac{1}{4}I_d & \omega t\in(\frac{\pi}{4}+\theta_3,\frac{\pi}{3}-\theta_3]\\ \frac{m_3}{2m_3+1}I_d & \omega t\in(\frac{\pi}{3}-\theta_3,\frac{\pi}{3}+\theta_3]\\ \frac{1}{4}I_d & \omega t\in(\frac{\pi}{3}+\theta_3,\frac{5\pi}{12}-\theta_3]\\ 0 & \omega t\in(\frac{5\pi}{12}-\theta_3,\frac{5\pi}{12}+\theta_3]\\ \frac{\sqrt{3}}{4}I_d & \omega t\in(\frac{5\pi}{12}+\theta_3,\frac{\pi}{2}-\theta_3]\\ \frac{\sqrt{3}m_3}{2m_3+1}I_d & \omega t\in(\frac{\pi}{2}-\theta_3,\frac{\pi}{2}+\theta_3]\\ \frac{\sqrt{3}}{4}I_d & \omega t\in(\frac{\pi}{2}+\theta_3,\frac{7\pi}{12}-\theta_3]\\ 0 & \omega t\in(\frac{7\pi}{12}-\theta_3,\frac{7\pi}{12}+\theta_3]\\ \frac{1}{4}I_d & \omega t\in(\frac{7\pi}{12}+\theta_3,\frac{2\pi}{3}-\theta_3]\\ \frac{m_3}{2m_3+1}I_d & \omega t\in(\frac{2\pi}{3}-\theta_3,\frac{2\pi}{3}]\end{cases},\quad i_{d12}=\begin{cases}\frac{m_3}{2m_3+1}I_d & \omega t\in(0,\theta_3]\\ \frac{1}{4}I_d & \omega t\in(\theta_3,\frac{\pi}{12}-\theta_3]\\ 0 & \omega t\in(\frac{\pi}{12}-\theta_3,\frac{\pi}{12}+\theta_3]\\ \frac{\sqrt{3}}{4}I_d & \omega t\in(\frac{\pi}{12}+\theta_3,\frac{\pi}{6}-\theta_3]\\ \frac{\sqrt{3}m_3}{2m_3+1}I_d & \omega t\in(\frac{\pi}{6}-\theta_3,\frac{\pi}{6}+\theta_3]\\ \frac{\sqrt{3}}{4}I_d & \omega t\in(\frac{\pi}{6}+\theta_3,\frac{\pi}{4}-\theta_3]\\ 0 & \omega t\in(\frac{\pi}{4}-\theta_3,\frac{\pi}{4}+\theta_3]\\ \frac{1}{4}I_d & \omega t\in(\frac{\pi}{4}+\theta_3,\frac{\pi}{3}-\theta_3]\\ \frac{m_3}{2m_3+1}I_d & \omega t\in(\frac{\pi}{3}-\theta_3,\frac{\pi}{3}+\theta_3]\\ \frac{1}{4}I_d & \omega t\in(\frac{\pi}{3}+\theta_3,\frac{5\pi}{12}-\theta_3]\\ 0 & \omega t\in(\frac{5\pi}{12}-\theta_3,\frac{7\pi}{12}+\theta_3]\\ \frac{1}{4}I_d & \omega t\in(\frac{7\pi}{12}+\theta_3,\frac{2\pi}{6}-\theta_3]\\ \frac{m_3}{2m_3+1}I_d & \omega t\in(\frac{2\pi}{3}-\theta_3,\frac{2\pi}{3}]\end{cases}\tag{A1}$$

$$i_{d21}=\begin{cases}0 & \omega t\in(0,\theta_3]\\ \frac{1}{4}I_d & \omega t\in(\theta_3,\frac{\pi}{12}-\theta_3]\\ \frac{m_3}{2m_3+1}I_d & \omega t\in(\frac{\pi}{12}-\theta_3,\frac{\pi}{12}+\theta_3]\\ \frac{1}{4}I_d & \omega t\in(\frac{\pi}{12}+\theta_3,\frac{\pi}{6}-\theta_3]\\ 0 & \omega t\in(\frac{\pi}{6}-\theta_3,\frac{\pi}{6}+\theta_3]\\ \frac{\sqrt{3}}{4}I_d & \omega t\in(\frac{\pi}{6}+\theta_3,\frac{\pi}{4}-\theta_3]\\ \frac{\sqrt{3}m_3}{2m_3+1}I_d & \omega t\in(\frac{\pi}{4}-\theta_3,\frac{\pi}{4}+\theta_3]\\ \frac{\sqrt{3}}{4}I_d & \omega t\in(\frac{\pi}{4}+\theta_3,\frac{\pi}{3}-\theta_3]\\ 0 & \omega t\in(\frac{\pi}{3}-\theta_3,\frac{\pi}{3}+\theta_3]\\ \frac{1}{4}I_d & \omega t\in(\frac{\pi}{3}+\theta_3,\frac{5\pi}{12}-\theta_3]\\ \frac{m_3}{2m_3+1}I_d & \omega t\in(\frac{5p}{12}-\theta_3,\frac{5\pi}{12}\pi+\theta_3]\\ \frac{1}{4}I_d & \omega t\in(\frac{5\pi}{12}+\theta_3,\frac{\pi}{2}-\theta_3]\\ 0 & \omega t\in(\frac{\pi}{2}-\theta_3,\frac{2\pi}{3}]\end{cases},\quad i_{d22}=\begin{cases}0 & \omega t\in(0,\theta_3]\\ \frac{1}{4}I_d & \omega t\in(\theta_3,\frac{\pi}{12}-\theta_3]\\ \frac{m_3}{2m_3+1}I_d & \omega t\in(\frac{\pi}{12}-\theta_3,\frac{\pi}{12}+\theta_3]\\ \frac{1}{4}I_d & \omega t\in(\frac{\pi}{12}+\theta_3,\frac{\pi}{6}-\theta_3]\\ 0 & \omega t\in(\frac{\pi}{6}-\theta_3,\frac{\pi}{3}+\theta_3]\\ \frac{1}{4}I_d & \omega t\in(\frac{\pi}{3}+\theta_3,\frac{5\pi}{12}-\theta_3]\\ \frac{m_3}{2m_3+1}I_d & \omega t\in(\frac{5\pi}{12}-\theta_3,\frac{5\pi}{12}+\theta_3]\\ \frac{1}{4}I_d & \omega t\in(\frac{5\pi}{12}+\theta_3,\frac{\pi}{2}-\theta_3]\\ 0 & \omega t\in(\frac{\pi}{2}-\theta_3,\frac{\pi}{2}+\theta_3]\\ \frac{\sqrt{3}}{4}I_d & \omega t\in(\frac{\pi}{2}+\theta_3,\frac{7\pi}{12}-\theta_3]\\ \frac{\sqrt{3}m_3}{2m_3+1}I_d & \omega t\in(\frac{7\pi}{12}-\theta_3,\frac{7\pi}{12}+\theta_3]\\ \frac{\sqrt{3}}{4}I_d & \omega t\in(\frac{7\pi}{12}+\theta_3,\frac{2\pi}{3}-\theta_3]\\ 0 & \omega t\in(\frac{2\pi}{3}-\theta_3,\frac{2\pi}{3}]\end{cases}\tag{A2}$$

$$i_{A1}=k\begin{cases}0 & \omega t\in(0,\theta_3]\\ 0 & \omega t\in(\theta_3,\frac{\pi}{12}-\theta_3]\\ 0 & \omega t\in(\frac{\pi}{12}-\theta_3,\frac{\pi}{12}+\theta_3]\\ \frac{\sqrt{3}}{12}I_d & \omega t\in(\frac{\pi}{12}+\theta_3,\frac{\pi}{6}-\theta_3]\\ \frac{\sqrt{3}}{3}\frac{m_3}{2m_3+1}I_d\omega t\in(\frac{\pi}{6}-\theta_3,\frac{\pi}{6}+\theta_3]\\ \frac{\sqrt{3}}{12}I_d\omega t\in(\frac{\pi}{6}+\theta_3,\frac{\pi}{4}-\theta_3]\\ 0\omega t\in(\frac{\pi}{4}-\theta_3,\frac{\pi}{4}+\theta_3]\\ \frac{1}{4}I_d\omega t\in(\frac{\pi}{4}+\theta_3,\frac{\pi}{3}-\theta_3]\\ \frac{m_3}{2m_3+1}I_d\omega t\in(\frac{\pi}{3}-\theta_3,\frac{\pi}{3}+\theta_3]\\ \frac{1}{4}I_d\omega t\in(\frac{\pi}{3}+\theta_3,\frac{5\pi}{12}-\theta_3]\\ 0\omega t\in(\frac{5\pi}{12}-\theta_3,\frac{5\pi}{12}+\theta_3]\\ \frac{\sqrt{3}}{6}I_d\omega t\in(\frac{5\pi}{12}+\theta_3,\frac{\pi}{2}-\theta_3]\\ \frac{\sqrt{3}}{3}\frac{2m_3}{2m_3+1}I_d\omega t\in(\frac{\pi}{2}-\theta_3,\frac{\pi}{2}]\end{cases}\quad i_{A2}=k\begin{cases}0 & \omega t\in(0,\theta_3]\\ k_2\frac{1}{4}I_d & \omega t\in(\theta_3,\frac{\pi}{12}-\theta_3]\\ k_2\frac{m_3}{2m_3+1}I_d & \omega t\in(\frac{\pi}{12}-\theta_3,\frac{\pi}{12}+\theta_3]\\ k_2\frac{1}{4}I_d & \omega t\in(\frac{\pi}{12}+\theta_3,\frac{\pi}{6}-\theta_3]\\ 0 & \omega t\in(\frac{\pi}{6}-\theta_3,\frac{\pi}{6}+\theta_3]\\ (k_2+\frac{1}{6})\frac{2\sqrt{3}+3}{2\sqrt{3}+4}\frac{1}{2}I_d & \omega t\in(\frac{\pi}{6}+\theta_3,\frac{\pi}{4}-\theta_3]\\ (k_2+\frac{1}{6})\frac{2\sqrt{3}+3}{2\sqrt{3}+4}\frac{2m_3}{2m_3+1}I_d & \omega t\in(\frac{\pi}{4}-\theta_3,\frac{\pi}{4}+\theta_3]\\ (k_2+\frac{1}{6})\frac{2\sqrt{3}+3}{2\sqrt{3}+4}\frac{1}{2}I_d & \omega t\in(\frac{\pi}{4}+\theta_3,\frac{\pi}{3}-\theta_3]\\ 0 & \omega t\in(\frac{\pi}{3}-\theta_3,\frac{\pi}{3}+\theta_3]\\ (k_2+k_3)\frac{1}{4}I_d & \omega t\in(\frac{\pi}{3}+\theta_3,\frac{5\pi}{12}-\theta_3]\\ (k_2+k_3)\frac{m_3}{2m_3+1}I_d & \omega t\in(\frac{5\pi}{12}-\theta_3,\frac{5\pi}{12}+\theta_3]\\ (k_2+k_3)\frac{1}{4}I_d & \omega t\in(\frac{5\pi}{12}+\theta_3,\frac{\pi}{2}-\theta_3]\\ 0 & \omega t\in(\frac{\pi}{2}-\theta_3,\frac{\pi}{2}]\end{cases}.\tag{A3}$$

REFERENCES

[1] H. Tian, M. Chen, G. Liang, and X. Xiao, "A single-phase transformerless common-ground type PV inverter with active power decoupling," *IEEE Trans. Ind. Electron.*, vol. 70, no. 4, pp. 3762–3772, Apr. 2023, doi: 10.1109/TIE.2022.3181361.

[2] H. Guo, D. Gong, L. Zhang, F. Wang, and D. Du, "Hierarchical game for low-carbon energy and transportation systems under dynamic hydrogen pricing," *IEEE Trans. Ind. Inform.*, vol. 19, no. 2, pp. 2008–2018, Feb. 2023, doi: 10.1109/TII.2022.3190550.

[3] S. Lai, J. Qiu, Y. Tao, X. Sun, and J. Zhao, "Charging/refueling navigation strategies for plug-in hybrid hydrogen and electric vehicles with irrationalities and energy substitution," *IEEE Trans. Ind. Inform.*, vol. 20, no. 1, pp. 583–595, Jan. 2024, doi: 10.1109/TII.2023.3268753.

[4] H. Tian et al., "Novel three-phase efficient power supply for hydrogen production using active voltage injection method," *IEEE Trans. Ind. Electron.*, early access, Aug. 13, 2025, doi: 10.1109/TIE.2025.3589459.

[5] L. Kong, J. Yu, and G. Cai, "Modeling, control and simulation of a photovoltaic /hydrogen/supercapacitor hybrid power generation system for grid-connected applications," *Int. J. Hydrogen Energy*, vol. 44, no. 46, pp. 25129–25144, 2019, doi: 10.1016/j.ijhydene.2019.05.097.

[6] P. Rullo et al., "Integration of sizing and energy management based on economic predictive control for standalone hybrid renewable energy systems," *Renew. Energy*, vol. 140, no. 9, pp. 436–451, 2019, doi: 10.1016/j.renene.2019.03.074.

[7] J. Koponen, V. Ruuskanen, A. Kosonen, M. Niemelä, and J. Ahola, "Effect of converter topology on the specific energy consumption of Alkaline water electrolyzers," *IEEE Trans. Power Electron.*, vol. 34, no. 7, pp. 6171–6182, Jul. 2019, doi: 10.1109/TPEL.2018.2876636.

[8] S. Wang, X. Ruan, and Y. He, "Unified small-signal impedance modeling and analysis of multi-pulse rectifier units for more electric aircraft," *IEEE Trans. Power Electron.*, vol. 39, no. 7, pp. 8610–8621, Jul. 2024, doi: 10.1109/TPEL.2024.3376688.

[9] A. Patel, S. Gupta, N. P. Singh, and U. K. Baruah, "Controlled rectifier for improved harmonic performance of a pulse step modulated high voltage power supply," *IEEE Trans. Plasma Sci.*, vol. 48, no. 12, pp. 4374–4380, Dec. 2020, doi: 10.1109/TPS.2020.3033839.

[10] H. Shi, Z. Zhang, J. Han, and J. Li, "Dynamic performance improvement of wound rotor synchronous starter/generator system based on PWM rectifier," *IEEE Trans. Transp. Electrific.*, vol. 9, no. 3, pp. 4639–4649, Sep. 2023, doi: 10.1109/TTE.2023.3247868.

[11] J. Zhu, H. Wu, J. Chen, L. Li, M. Hua, and Y. Xing, "A hybrid three-phase AC/DC power system for low-frequency pulsed load applications," *IEEE Trans. Ind. Electron.*, vol. 68, no. 3, pp. 1871–1882, Mar. 2021, doi: 10.1109/TIE.2020.2977575.

[12] J. Won, S. Srdic, and S. M. Lukic, "Optimized multi-carrier PWM strategy and topology review for multi-cell series-parallel medium-voltage rectifier," *IEEE J. Emerg. Sel. Topics Power Electron.*, vol. 10, no. 6, pp. 6770–6783, Dec. 2022, doi: 10.1109/JESTPE.2021.3129797.

[13] Q. Du, W. Liu, Q. Li, L. Gao, and F. Meng, "A series-connected 40-pulse rectifier with DC link passive harmonic reduction circuit," *IEEE Trans. Power Electron.*, vol. 37, no. 3, pp. 3007–3023, Mar. 2022, doi: 10.1109/TPEL.2021.3110976.

[14] J. Wang, C. Zhao, T. Yu, T. Liu, X. Yao, and Q. Chen, "New 24-pulse rectifier with passive current injection circuit based on dual auxiliary transformers," *IEEE J. Emerg. Sel. Topics Power Electron.*, vol. 11, no. 5, pp. 5321–5336, Oct. 2023, doi: 10.1109/JESTPE.2023.3308188.

[15] J. Wang, Y. Lv, L. Li, X. Yao, Q. Guan, and Q. Chen, "A 24-pulse rectifier with a passive auxiliary current injection circuit at DC side," *IEEE Trans. Power Electron.*, vol. 37, no. 9, pp. 11109–11123, Sep. 2022, doi: 10.1109/TPEL.2022.3160944.

[16] P. P. S., R. Kalpana, K. S. Chethana, and B. Singh, "A 36-pulse AC–DC converter with DC-side tapped interphase bridge rectifier for power quality improvement," *IEEE Trans. Ind. Appl.*, vol. 57, no. 1, pp. 549–558, Jan./Feb. 2021, doi: 10.1109/TIA.2020.3028341.

[17] H. Tian et al., “High-efficiency asymmetrically designed three-phase virtual 48-pulse power supply for electrolytic hydrogen,” *IEEE Trans. Power Electron.*, vol. 40, no. 8, pp. 10335–10342, Aug. 2025, doi: 10.1109/TPEL.2025.3552068.

[18] R. Abdollahi, A. Salemnia, G. B. Gharehpetian, and M. Davari, “A parallel-connected 40-pulse diode rectifier with DC-link passive pulse multiplication circuit,” *IEEE Trans. Ind. Electron.*,„ vol. 71, no. 7, pp. 6556–6567, Jul. 2024, doi: 10.1109/TIE.2023.3296822.

[19] R. Abdollahi, G. B. Gharehpetian, and M. Davari, “A novel more electric aircraft power system rectifier based on a low-rating autotransformer,” *IEEE Trans. Transp. Electrific.*, vol. 8, no. 1, pp. 649–659, Mar. 2022, doi: 10.1109/TTE.2021.3104576.

[20] H. Tian, W. Han, J. Sathik M, M. Chen, G. Liang, and S. Mekhilef, “High-efficiency, High-power asymmetrically designed three-phase power supply for electrolytic hydrogen production,” *IEEE Trans. Power Electron.*, vol. 40, no. 1, pp. 92–97, Jan. 2025, doi: 10.1109/TPEL.2024.3464675.

[21] Y. Lian, S. Yang, and W. Yang, “Optimum design of 48-pulse rectifier using unconventional interphase reactor,” *IEEE Access*, vol. 7, pp. 61240–61250, 2019, doi: 10.1109/ACCESS.2019.2902453.

[22] J. Wang, T. Liu, T. Yu, C. Zhao, X. Yao, and Q. Chen, “A series-connected 24-pulse star rectifier employing two different pulse-doubling interphase reactors,” *IEEE Trans. Power Electron.*, vol. 39, no. 1, pp. 1460–1481, Jan. 2024, doi: 10.1109/TPEL.2023.3323795.

[23] Q. Li, F. Meng, L. Gao, H. Zhang, and Q. Du, “A 30-pulse rectifier using passive voltage harmonic injection method at DC link,” *IEEE Trans. Ind. Electron.*, vol. 67, no. 11, pp. 9273–9291, Nov. 2020, doi: 10.1109/TIE.2019.2956404.

[24] M. S. Akther, F. Afreen Nishat, M. M. Alam, R. Parvin Mou, and M. S. Ali, “A unique 48-pulse passive rectifier for harmonics compensation,” in *Proc. IEEE Int. Women Eng. Conf. Elect. Comput. Eng.*, 2020, pp. 1–4, doi: 10.1109/WIECON-ECE52138.2020.9397937.

[25] J. Chen, H. Bai, J. Chen, and C. Gong, “A novel parallel configured 48-pulse autotransformer rectifier for aviation application,” *IEEE Trans. Power Electron.*, vol. 37, no. 2, pp. 2125–2138, Feb. 2022, doi: 10.1109/TPEL.2021.3106322.

Hanlei Tian (Student Member, IEEE) was born in Shijiazhuang, China. He received the M.S. degree in electrical engineering from the University of Science and Technology of Hebei, Shijiazikhuang, China, in 2016. He is currently working toward the doctoral degree with The Hong Kong University of Science and Technology, Guangzhou, China.

From 2016 to 2019, he was a cocultured student with the Electric Power College, South China University of Technology, Guangzhou, China. He has authored or coauthored more than 30 technical papers. His research interests include high-frequency power converters, renewable energy conversion systems, grid-connected converters, modeling and control of converters.

Guozhuang Liang (Member, IEEE) received the M.S. degree in electrical engineering from the Hebei University of Technology, Tianjin, China, in 1999. He is currently working toward the Ph.D. degree in control engineering with the University of the West of England, Bristol, U.K.

He is currently an Professor and the Vice-Dean with the School of Electrical Engineering, Hebei University of Science and Technology. His research interests include power electronics application, electrical detection, and information processing technology.

Jinliang Huang (Student Member, IEEE) was born in Shantou, China. He received the B.Sc. degree in electrical engineering from the Dongguan University of Technology, Dongguan, China, in 2020, and the M.S. degree in electrical engineering from Guangdong University of Technology, Guangzhou, China, in 2023. He is currently working toward the Ph.D. degree in electrical engineering with the Hong Kong University of Science and Technology, Guangzhou, China.

His research interests include multilevel inverter, switched-capacitor converter, and high-conversion ratio converter.

Junyu Fan received the B.S. degree in electrical engineering and automation from Dalian Maritime University, Dalian, China, in 2019, and the M.S. degree in electronic information from Southeast University, Nanjing, China, in 2022. He is currently working toward the Ph.D. degree in sustainable energy and environment with the Sustainable Energy and Environment Thrust, Hong Kong University of Science and Technology, Guangzhou, China.

His research interests include the control and analysis of ultrasonic motors and wireless power transfer.

Bowang Zhang received the B.S. degree in electrical engineering from Southeast University, Nanjing, China, in 2019, and the M.S. degree in electrical engineering from National Taiwan University, Taipei, Taiwan, in 2022. He is currently working toward the Ph.D. degree in sustainable energy and environment with The Hong Kong University of Science and Technology, Gaungzhou, China.

His research interests include power electronics and wireless power transfer.

Peisong Han received the bachelore’s and M.S. degree from Hebei University of Science and Technology, Shijiazhuang, China, in 2021 and 2024, respectively. He is currently working toward the Ph.D. degree in electrical engineering with Yanshan University, Qinhuangdao, China.

His research interests include renewable energy systems, high-frequency power converters, and power electronic converter design and control.

Maolin Chen (Member, IEEE) was born in Chongqing, China, in 1998. He received the B.S. and M.Sc. degrees in electrical engineering from Sichuan University, Chengdu, China, in 2020 and 2023, respectively.

He is currently an Assistant Researcher with Hong Kong University of Science and Technology, Hong Kong. He has authored or coauthored six technical papers. His research interests include the renewable energy based electrolytic hydrogen production, converter topology and control technology.

Wei Han (Member, IEEE) received the M.Sc. and Ph.D. degrees in electrical and electronic engineering from The University of Hong Kong, Hong Kong, in 2015 and 2020, respectively.

In 2021, he was a Postdoctoral Fellow with the University of Toronto. He is currently an Assistant Professor with the Sustainable Energy and Environment Thrust, Hong Kong University of Science and Technology, Guangzhou, China. He is also an Affiliated Assistant Professor with the Department of Electronic & Computer Engineering, The Hong Kong University of Science and Technology, Hong Kong. He has authored or coauthored an English book, more than 90 journal and conference papers in the fields of power electronics, wireless power transfer, motor drives and microgrids. He is also listed in the Stanford/Elsevier-Top 2% Scientists List, acts as an Associate Editors of Scientific Reports and Applied Sciences.